

Rotational states and shapes of Ryugu and Bennu:

Implications for interior structure and strength

J.H. Roberts^{1*}, O.S. Barnouin¹, M.G. Daly², K.J. Walsh³, M.C. Nolan⁴, R.T. Daly¹, P. Michel⁵,
Y. Zhang⁵, M.E. Perry¹, G.A. Neumann⁶, J.A. Seabrook², R.W. Gaskell⁷, E.E. Palmer⁷, J.R.
Weirich⁷, S. Watanabe^{8,9}, N. Hirata¹⁰, Na. Hirata¹¹, S. Sugita¹², D.J. Scheeres¹³, J.W.
McMahon¹³, D.S. Lauretta⁴

¹Johns Hopkins University Applied Physics Laboratory, Laurel, MD, USA; ²The Centre for Research in Earth and Space Science, York Univ., Toronto, Ontario, Canada; ³Southwest Research Institute, Boulder, CO, USA; ⁴Lunar and Planetary Laboratory, University of Arizona, Tucson, AZ, USA; ⁵Université Côte d'Azur, Observatoire de la Côte d'Azur, CNRS, Laboratoire Lagrange, Nice, France; ⁶NASA Goddard Space Flight Center, Greenbelt, MD, USA; ⁷Planetary Science Institute, Tucson, AZ, USA; ⁸Nagoya Univ., Nagoya, Japan; ⁹Institute of Space and Astronautical Science, JAXA, Sagami-hara, Japan; ¹⁰Univ. of Aizu, Aizu-Wakamatsu, Japan; ¹¹Kobe Univ., Kobe, Japan; ¹²Univ. of Tokyo, Tokyo, Japan; ¹³Department of Aerospace Engineering, University of Colorado, Boulder, CO, USA.

*Corresponding Author E-mail address: James.Roberts@jhuapl.edu

Submitted to Planetary and Space Science: 06 April 2021

Manuscript pages: 42 (including abstract)

Tables: 3

Figures: 13

Proposed running head: Rotational states and shapes of Ryugu and Bennu

Editorial correspondence:

James H. Roberts

The Johns Hopkins University Applied Physics Laboratory

11100 Johns Hopkins Road

Laurel, MD 20723-6099, USA

Email: James.Roberts@jhuapl.edu

Phone: (240) 228-9133

Fax: (240) 228-8939

1 **Keywords:** Ryugu, Bennu, Asteroids, Rotational Dynamics, Shape Model

2

3 **ABSTRACT**

4 Images of asteroids (162173) Ryugu and (101955) Bennu acquired by the Hayabusa2
5 and OSIRIS-REx missions, respectively, reveal rocky worlds covered in rubble. These
6 two asteroids do not have hydrostatic shapes, indicating that they possess some internal
7 friction and/or cohesion even if they lack tensile strength. Understanding the deviation of
8 the surfaces of these bodies from those of idealized shapes helps constrain the mechanical
9 properties of their interiors. Here, we focus on the feedback between YORP-induced
10 spin-up (in which asymmetric reflection and re-emission of solar radiation from the
11 surface systematically change the rotation rate), long-wavelength topography (which
12 provides a structure to control the orientation), and surface roughness on Ryugu and
13 Bennu. By performing spherical harmonic analyses of the shapes of these two asteroids,
14 we find that although they are superficially similar, they exhibit different long-
15 wavelength topography that implies different internal structures and rotational histories.
16 Bennu's shape and rotation rate require a modest amount of internal strength through
17 some combination of at least 17° of internal friction or a few Pa of cohesion, whereas
18 Ryugu could be nearly strengthless. Bennu's longitudinal ridges make it susceptible to
19 YORP spin-up, consistent with the observed increase in rotation rate that is not seen on
20 Ryugu. These longitudinal ridges also suggest a heterogeneous density structure for
21 Bennu, consistent with gravity data.

22

23

24 **1. Introduction**

25 At first glance, the asteroids (162173) Ryugu and (101955) Bennu look similar.
26 Images acquired by the Hayabusa2 (Watanabe et al., 2019) and OSIRIS-REx (Origins,
27 Spectral Interpretation, Resource Identification, and Security–Regolith Explorer)
28 (DellaGuistina and Emery et al., 2019; Walsh et al., 2019) missions reveal that both are
29 rocky worlds covered in rubble, including numerous boulders with diameters of tens of
30 meters or larger. Both bodies have low albedos and spectra consistent with a carbonaceous
31 chondrite–like composition (Watanabe et al., 2019; DellaGuistina and Emery et al., 2019;
32 Hamilton et al., 2019). To first order, both are shaped like spinning tops (Barnouin et al.,
33 2019a; Watanabe et al., 2019). Their shapes are not hydrostatic, so they must possess some
34 level of internal friction and/or cohesion even if they have no tensile strength (Zhang et al.,
35 2017; Hirabayashi and Scheeres, 2015). Understanding the deviation of the shapes from
36 idealized surfaces can therefore help constrain the mechanical properties of the two
37 asteroids’ interiors.

38 Shape models of Ryugu and Bennu have been developed from spacecraft images
39 using multiple techniques, including stereophotoclinometry (SPC) (Gaskell et al., 2008b;
40 Barnouin et al., 2019a, 2020) and geometric stereo (SfM) (Hirata et al., 2018), as well as
41 from lidar ranging data collected by the OSIRIS-REx Laser Altimeter (OLA) (Daly et al.,
42 2017, 2020; Barnouin et al., 2020) in the case of Bennu. Examples of shape models of
43 Bennu and Ryugu are shown in Figure 1.

44 The rotational states and shapes of these bodies are key to understand their histories
45 and predict future dynamic evolutions. The geologic evolution of rubble-pile asteroids is
46 driven in large part by migration of surface material (Walsh et al., 2008, 2012; Harris et

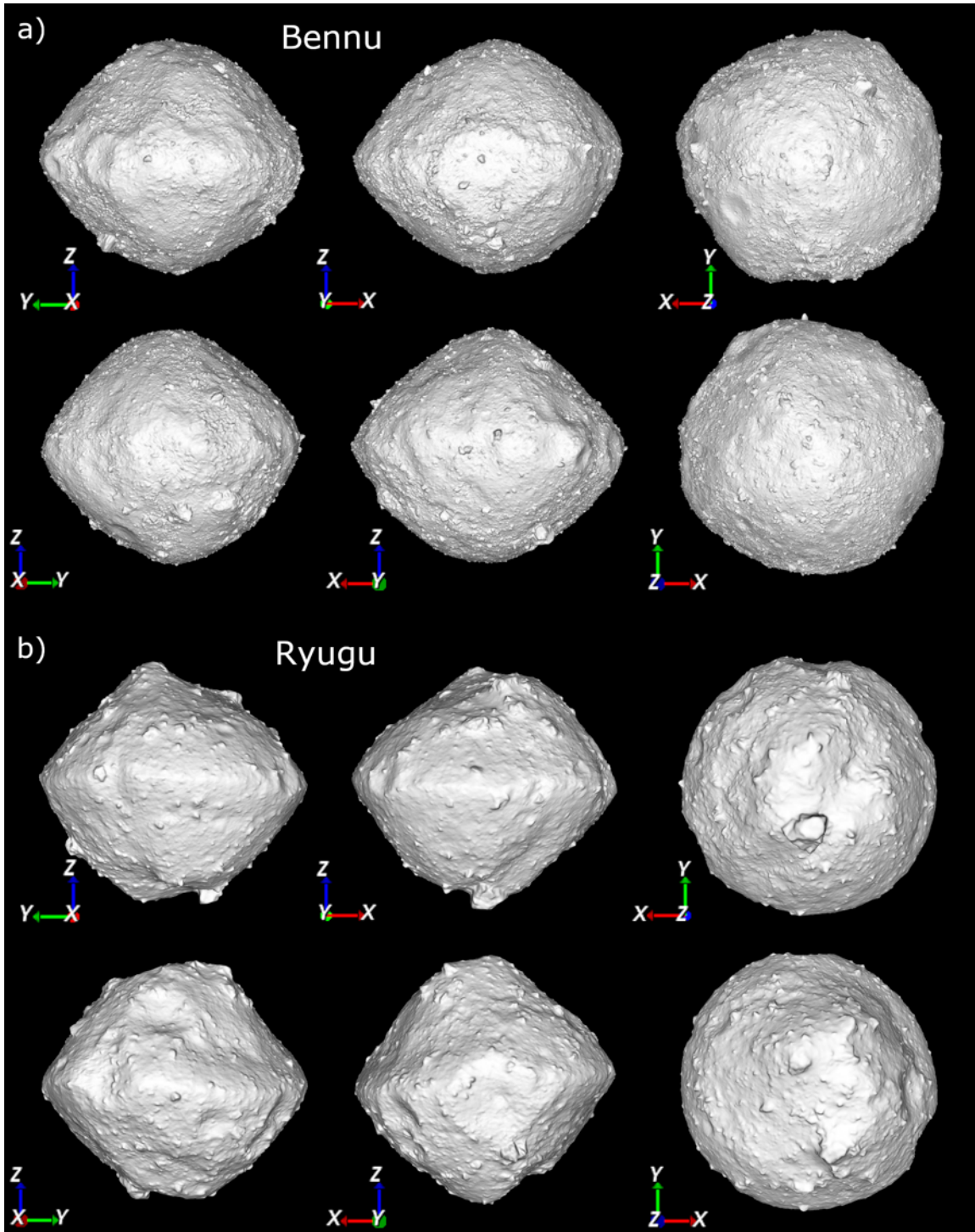


Figure 1: Example shape models of Benu (a) and Ryugu (b), each with ~800,000 facets. Views are shown from each principal axis. Benu model v20 was determined from laser altimetry data acquired by OLA. Ryugu model v20190802 was determined using stereophotoclinometry from imaging data collected by Hayabusa2 (Watanabe et al., 2019). For scale, the mean equatorial diameters of Benu and Ryugu are 557 m and 1.02 km, respectively.

47 al., 2009; Richardson and Bowling, 2014), which may be dislodged by a suite of processes

48 including re-accumulation (Michel and Ballouz et al., 2020; Holsapple, 2004), impact-
49 induced surface changes, and thermally driven processes (Dombard et al., 2010; Delbo et
50 al. 2014; Molaro et al. 2020) that include thermal fragmentation. Sub-kilometer bodies are
51 susceptible to changes in rotation due to the Yarkovsky–O’Keefe–Radzievskii–Paddack
52 (YORP) effect (Rubincam, 2000; Walsh et al., 2008; Cotto-Figueroa et al., 2015), in
53 which asymmetric reflection, absorption, and re-emission of solar radiation from the
54 surface cause torques that systematically increase or decrease the spin.

55 Benu rotates with a period of 4.3 hours (Hergenrother et al., 2019), nearly twice
56 as rapidly as Ryugu, which has a 7.6-hour rotational period (Watanabe et al., 2019). The
57 rotation rate of Benu has been observed to increase (Nolan et al., 2019; Hergenrother et
58 al., 2019) since its discovery in 1999, at a rate of $2.7 \times 10^{-4} \text{ rad s}^{-1} \text{ Myr}^{-1}$, which, if sustained,
59 would double the rotation rate every 1.5 Myr (Scheeres et al., 2019). The rotation of Ryugu
60 has not been observed to increase in this way; however, the baseline for observations is
61 much shorter than for Benu, and detection of YORP of a similar magnitude on Ryugu is
62 not feasible. The asteroids also have different sizes: Ryugu, with a mean diameter of 850
63 m, is much larger than Benu at 490 m. Ryugu thus has higher self-gravity and moment of
64 inertia, rendering it less susceptible to YORP torques and rotation-related deformation than
65 its smaller counterpart. The rotational and size properties of these two asteroids that are
66 important controls on their sensitivity to YORP are summarized in Table 1.

67 The shapes of these asteroids may reveal information about their interior
68 mechanical properties and implications for their dynamical evolution. Although some
69 differences in the shapes of Ryugu and Benu are immediately apparent, identification of
70 important features by eye is challenging, and subsequent interpretation could thus be

Table 1: Global physical properties of Benu and Ryugu

Physical Property		Benu	Ryugu	Units
Rotation Period	P	4.296057 ± 0.000002^a	7.63262 ± 0.00002^c	h
Mass	m	$7.329 \pm 0.009 \times 10^{10}^b$	$4.50 \pm 0.06 \times 10^{11}^c$	kg
Density	ρ	1190 ± 13^a	1190 ± 20^c	kg m^{-3}
Polar moment of Inertia	I_{zz}	26780^b	--	m^2
Major axis	a	505.56 ± 0.10^a	1023 ± 2^c	m
Median axis	b	492.4 ± 0.18^a	986 ± 4^c	m
Minor axis	c	457.38 ± 0.24^a	438 ± 2^c	m
Surface gravity	g	$5.95 \pm 0.01 \times 10^{-5}$ (mean) ^a	1.403×10^{-4} (equator) ^c 1.473×10^{-4} (poles) ^c	m s^{-2}

^a Barnouin et al. (2019a)^b Scheeres et al. (2019)^c Watanabe et al. (2019)

71 subjective. Here we perform spherical harmonic decompositions of the two asteroids’
72 shapes to quantify the patterns at a variety of length scales. In section 2, we briefly describe
73 the rotational stability of cohesionless rubble-pile bodies and relate the rotation periods to
74 the long-wavelength shapes, so that we have a baseline equilibrium shape against which to
75 compare the actual shapes of Benu and Ryugu. In section 3, we present a detailed
76 spherical harmonic analysis of the shapes of these two bodies, and in section 4 we relate
77 their observed long-wavelength topography to their internal strengths and interior
78 structures. In section 5, we discuss how observed topography contributes to spin evolution.
79 Because observations of a sustained increase in rotation rate exist for Benu (Nolan et al.,
80 2019; Hergenrother et al., 2019), but not for Ryugu, we take a deeper dive into the spin
81 evolution of Benu and show how its distinctive long-wavelength shape may be
82 particularly susceptible to YORP spin-up.

83

84

85 **2. Rotational Stability**

86 *2.1 Equilibrium Figures*

87 The simplest model of a rotating figure is a Maclaurin spheroid, which is an
88 oblate spheroid that arises when a fluid, self-gravitating body of uniform density rotates
89 with a constant angular velocity. To first order, these approximations of density and
90 angular velocity are appropriate for small rubble-pile asteroids. Although rubble piles are
91 not fluids, the relationship can be generalized to cohesionless solids with an internal
92 friction angle (Holsapple, 2004). The maximum stable spin rate Ω is a function of the
93 friction angle ϕ and the ratio α of the lengths of the polar axis C and equatorial axis A :

$$94 \quad \frac{\Omega^2}{\pi G \rho} = \frac{2\alpha\sqrt{m+2\alpha^2}}{m(1-\alpha^2)^{3/2}} \cos^{-1} \alpha - \frac{2(m+2)\alpha^2}{m(1-\alpha^2)}$$

95 where G is the gravitational constant, ρ is the density, and

$$96 \quad m = \frac{(1 + \sin \phi)}{(1 - \sin \phi)}$$

97 As the friction angle increases, higher spin rates can be supported without
98 deformation. In Figure 2, we plot the Maclaurin curves for several friction angles,
99 illustrating the maximum stable dimensionless spin rate as a function of axis ratio. Over
100 this, we plot the present states of Ryugu and Bennu, as well as three other representative
101 asteroids for which we have high-resolution shape models, and which can be
102 approximated as Maclaurin bodies. Because these bodies are not perfectly oblate, we
103 have used the mean equatorial axis when calculating α . Not shown are corresponding
104 curves for the minimum stable spin rates, which are relevant for extremely slow rotators.
105 The physical properties of the asteroids and their associated references are reported in
106 Table 2. There are many other asteroids for which radar shape models exists (e.g., Walsh

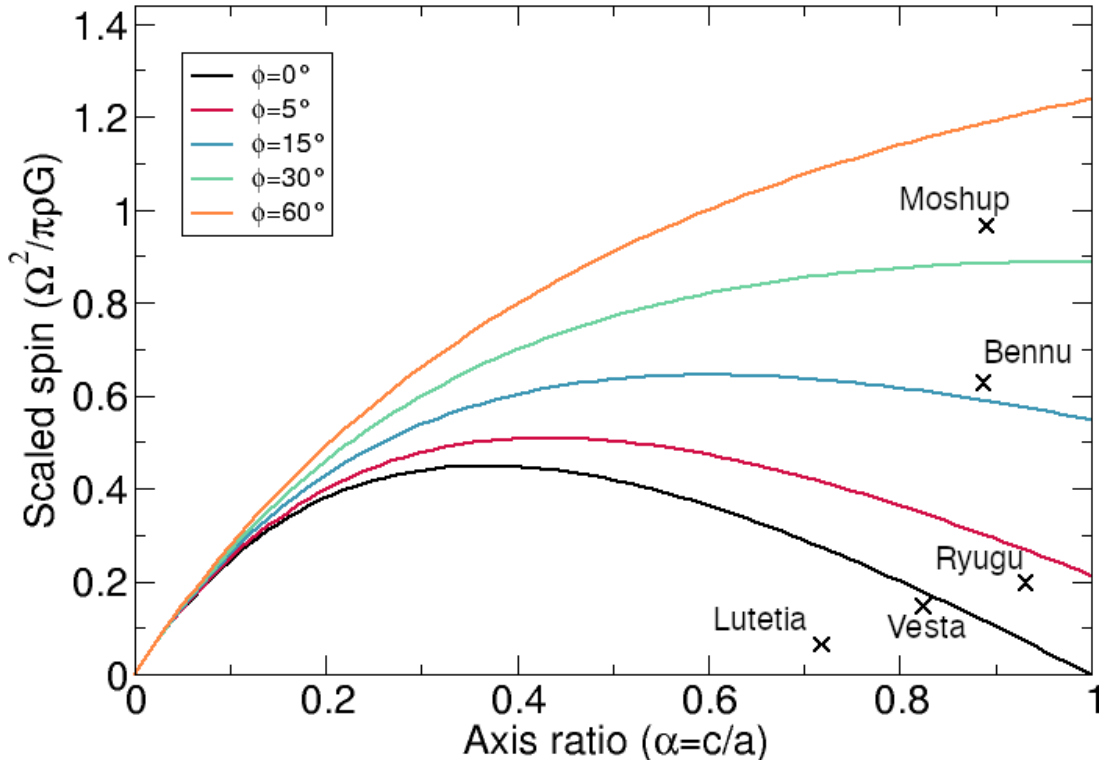


Figure 2: Rotational stability for cohesionless, solid, oblate spheroids for a wide range of rotation rates, oblateness, and internal friction. Each curve describes the limits of the allowable dimensionless rotation rate as a function of the axis ratio. The crosses mark the dimensionless spin rates and axis ratios consistent with observed oblate asteroids.

107 2018); however, we have chosen the ones with high-quality image-based shape models
 108 available from the Planetary Data System (PDS) as the most relevant comparisons to
 109 Bennu and Ryugu. We have also included (66391) Moshup, the first known top-shaped
 110 asteroid (Ostro et al., 2006), for comparison.

111 An object with the observed rotation rate and density of Bennu (Table 2) (Lauretta
 112 et al., 2019; Barnouin et al., 2019a, Scheeres et al., 2019, Hergenrother et al., 2019; Daly
 113 et al., 2020) requires $\phi > 17^\circ$ in the absence of cohesion. Alternatively, cohesion c could
 114 provide some tensile strength, reducing or eliminating the internal friction required.
 115 Internal friction is related to cohesion through the Factor of Safety (Das, 2010), which is a
 116 ratio of the frictional or cohesive forces to the driving forces:

Table 2: Physical properties relevant to rotational stability of 10 asteroids, here approximated as either oblate (Maclaurin) or prolate spheroids. Asteroids denoted by an asterisk are better approximated as tri-axial ellipsoids, but for this comparison have been classified as oblate or prolate. α , ratio of the lengths of the polar and equatorial axes. Ω , maximum stable spin rate. ρ , density.

Asteroid	Spheroid	α	Ω (s ⁻¹)	Period (hr)	ρ (kg m ⁻³)	Reference
(4) Vesta	Maclaurin	0.8242	3.27×10^{-4}	5.342	3.456×10^3	Gaskell (2013)
(21) Lutetia	Maclaurin*	0.7182	2.14×10^{-4}	8.166	3.4×10^3	Farnham (2013)
(243) Ida	Prolate	0.3679	3.77×10^{-4}	4.63	2.6×10^3	Stooke (2002)
(253) Mathilde	Prolate	0.7121	4.18×10^{-6}	417.7	1.3×10^3	Stooke (2002)
(433) Eros	Prolate	0.6512	3.31×10^{-4}	5.27	2.67×10^3	Gaskell (2008)
(951) Gaspra	Prolate	0.5330	2.48×10^{-4}	7.042	2.7×10^3	Stooke (2002)
(25143) Itokawa	Prolate*	0.4701	1.44×10^{-4}	12.132	1.95×10^3	Gaskell et al. (2008b)
(66391) Moshup	Maclaurin	0.8907	6.31×10^{-4}	2.765	2×10^3	Ostro et al. (2006)
(101955) Bennu	Maclaurin	0.8874	4.07×10^{-4}	4.296	1.19×10^3	Barnouin et al. (2019a)
(162173) Ryugu	Maclaurin	0.9317	2.29×10^{-4}	7.627	1.27×10^3	Watanabe et al. (2019)

$$117 \quad F_{friction} = \frac{\tan \phi}{\tan \theta}; \quad F_{cohesion} = \frac{c}{\rho g h \sin \theta}$$

118 where g is the surface gravity, θ is the slope, and h is the thickness of the regolith layer.

119 On Bennu, with a gravity of 6 micro-g and a density of 1.19 g cm^{-3} , 6 Pa of cohesion

120 would be sufficient to maintain the shape without internal friction (the presence of a solid

121 core at depth could reduce h and therefore the required c), although evidence of mass

122 migration at the surface (Jawin et al., 2020; Barnouin et al., 2019a; Walsh et al., 2019)

123 suggests that cohesion is probably minimal. Some combination of these levels of internal

124 friction or cohesion is required to prevent further flattening, despinning, and, potentially,

125 binary fission.

126 Although Ryugu has a similar overall shape, its lower rotation rate indicates that it

127 is much closer than Bennu to the Maclaurin curve (Figure 2), and only a very small

128 amount of internal friction ($\phi > 3^\circ$) or ~ 2 Pa of cohesion would be necessary to maintain
 129 its shape.

130 Not all asteroids are well approximated as a deviation from an oblate spheroid.
 131 Similar relationships exist for prolate spheroids, albeit with more complicated functions
 132 of friction angle and axis ratio. The scaled spin for these bodies is:

$$133 \quad \frac{\Omega^2}{\pi G \rho} = \frac{2 \lambda_x A_x + \lambda_y \beta^2 A_y + \lambda_z \alpha^2 A_z}{\lambda_x + \lambda_y \beta^2}$$

134 where β is the ratio between the short and long equatorial axes b and a . For a prolate
 135 body, $\alpha = \beta$. The constants λ_i have the values -1 , 0 , and m (as defined for the Maclaurin
 136 case), ordered according to the minimum, intermediate, and maximum stress directions.
 137 The coefficients A_i are log functions (Holsapple, 2004):

$$138 \quad A_x = \frac{b^2 \left[-4\sqrt{(a^2 - b^2)} + 4a \tanh^{-1} \left(\frac{a}{\sqrt{(a^2 - b^2)}} \right) + 2a \log \left(-1/\sqrt{(a^2 - b^2)} \right) + a \log (a^2 - b^2) \right]}{2(a^2 - b^2)^{\frac{3}{2}}}$$

$$139 \quad A_y = A_z =$$

$$140 \quad = \frac{-a \left[-4a\sqrt{(a^2 - b^2)} + 4b^2 \tanh^{-1} \left(\frac{a}{\sqrt{(a^2 - b^2)}} \right) + 2b^2 \log \left(-1/\sqrt{(a^2 - b^2)} \right) + b^2 \log (a^2 - b^2) \right]}{4(a^2 - b^2)^{\frac{3}{2}}}$$

141
 142 The upper curve is determined by the lower of the solutions where the stress in the z -
 143 direction (along the rotation axis) is the most negative. The lower curve is the solution
 144 where the stress in the x -direction (along the prolate bulge) is the most negative.

145 One complexity is that there are no stable situations for strengthless prolate
 146 spheroids (except in the degenerate case of a sphere). We have illustrated this in Figure 3,
 147 superposed with values for five prolate asteroids for which high-resolution shape models
 148 are available (Table 2). For very low (but finite) internal friction angles ($\phi < 6^\circ$), there

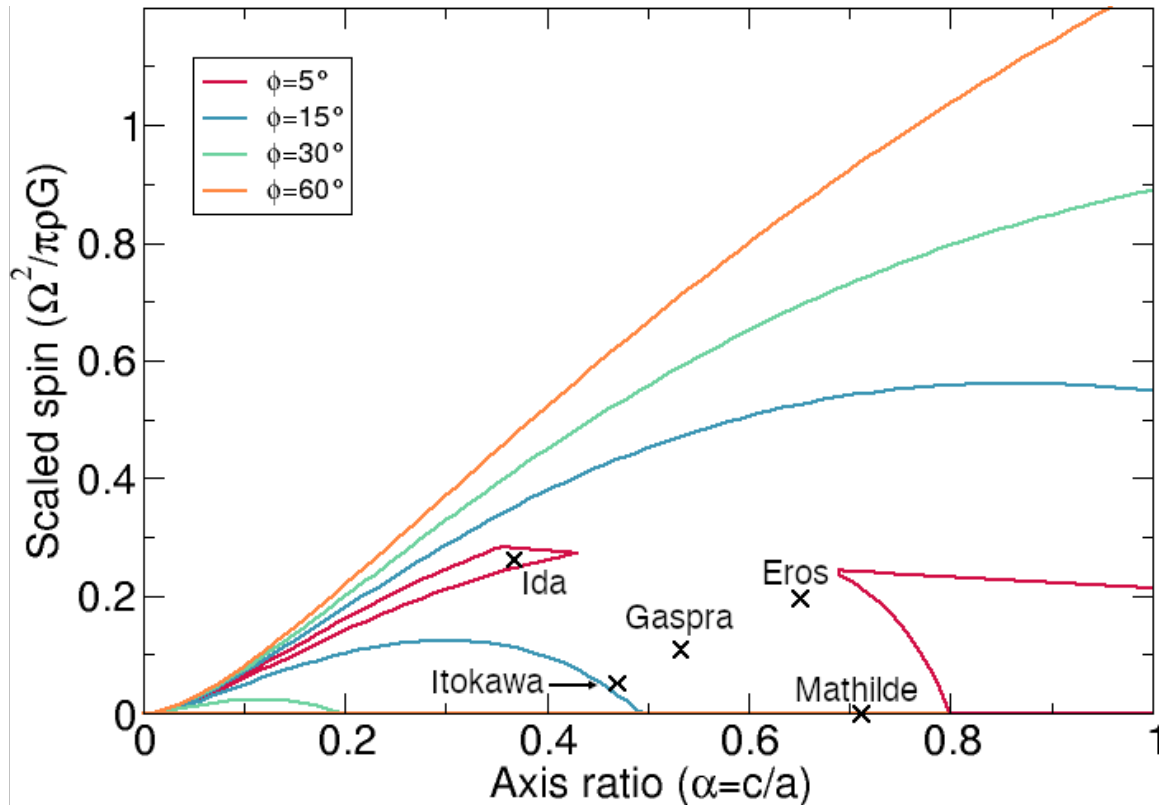


Figure 3: Rotational stability for cohesionless, solid, prolate spheroids for a wide range of rotation rate, prolateness, and internal friction. Each curve describes the limits of the allowable dimensionless rotation rate as a function of the axis ratio. Two curves of the same color denote the upper and lower bound of rotational stability and the indicated friction angle. Note that the stability region at a friction angle of 5° is discontinuous. The crosses mark the dimensionless spin rates and axis ratios consistent with observed prolate asteroids.

149 are stable regions for nearly spherical and very elongated bodies (red curve in Figure 3),
 150 and at higher friction angles, there are both upper and lower bounds on the rotation rate.

151 Although neither Bennu nor Ryugu have a prolate shape, the rotational stability
 152 analysis of prolate bodies may still be instructive. Itokawa, for example, may be most
 153 similar to Bennu in terms of its internal properties. It is a rubble pile asteroid as well
 154 (Fujiwara et al., 2006), but, as shown in Figure 3, requires nearly 15° of internal friction
 155 to maintain this rotational state and shape. The variable densities of the two lobes
 156 (Kanamaru et al., 2019) may indicate the presence of some larger fragments in the
 157 interior that have inherent strength, consistent with findings for Bennu (Daly et al., 2020;
 158 Scheeres et al., 2020).

159 In contrast, Ryugu does not require much strength and may consist of relatively
160 homogenous rubble throughout its interior. Likewise, the other prolate asteroids
161 examined here have scaled spin rates that do not require substantial strength, although all
162 prolate bodies require some finite internal friction or cohesion to maintain their shape.
163 Finite element analysis to determine the cohesion necessary to prevent failure of asteroids
164 under rotation results in failure mode diagrams (Hirabayashi and Scheeres, 2016). An
165 analysis of these failure mode diagrams has been done for several contact-binary,
166 elongated, and spheroidal asteroids, including Bennu and Itokawa (Hirabayashi and
167 Scheeres, 2019). Assuming friction angles of 35° (common for granular materials), these
168 bodies would require cohesion to prevent failure once the the peak centrifugal stress
169 balances the local gravity. This occurs at somewhat faster rotation periods than at present
170 (3.7 h and 5.73 h, for Bennu and Itokawa respectively). At faster spin rates, tens of Pa of
171 cohesion would be required to prevent failure (Hirabayashi and Scheeres, 2019).

172

173 2.2 Deviation from Equilibrium Figures

174 Having established the range of equilibrium figures (i.e., the shapes these bodies
175 would take on if they were fluids or frictionless granular material), it is instructive to
176 examine their deviations from these idealized surfaces (i.e., the difference between their
177 real shapes and the black curve in Figure 2). For each body, we took the equatorial radius
178 (257.5 m for Bennu (Barnouin et al., 2019); 501 m for Ryugu (Watanabe et al., 2019))
179 defined a reference spheroid consistent with the axis ratio α given in Table 2. In Figure 4,
180 we show the shape models of Bennu (derived from ranges obtained by OLA) and Ryugu

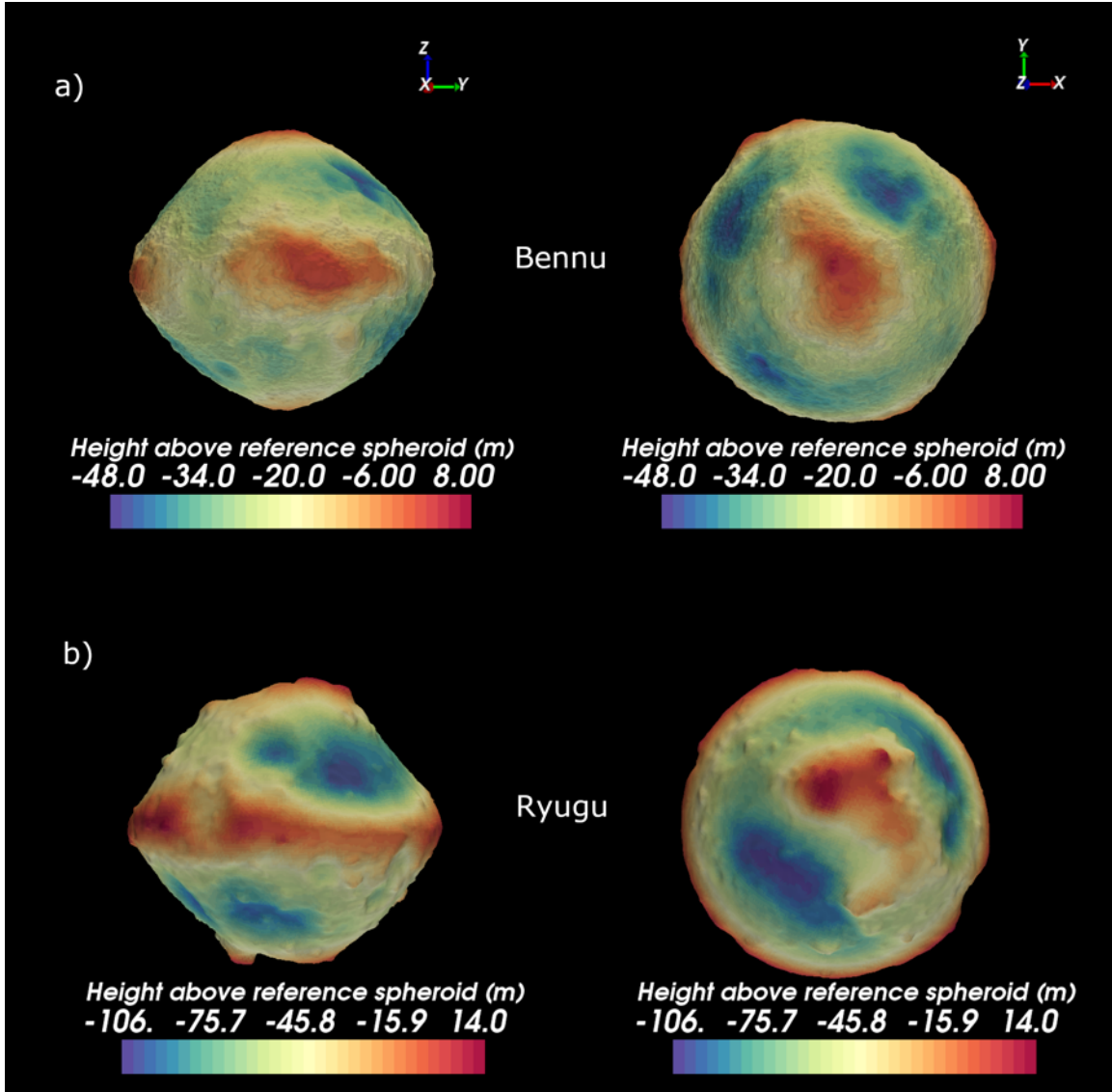


Figure 4: Deviation of Bennu's (a) and Ryugu's (b) shape models from the reference (i.e., closest-fit Maclaurin) spheroids, consistent with the asteroids' observed densities and rotation periods. Left: Equatorial view. Right: Polar view. Note that the color scales for Bennu and Ryugu have different ranges.

181 (derived from SPC), colored according to the height of the surface above a reference
 182 spheroid consistent with the axis ratio.

183 When scaled by their respective radii, the deviations of Bennu and Ryugu from
 184 their respective equilibrium figures are similar. The most prominent features that deviate
 185 from the equilibrium figures on these bodies are their equatorial bulges and their equatorial
 186 ridges. Although similar-sounding, these equatorial features have different origins and

187 expressions. The equatorial bulge arises through centrifugal force that is a natural
188 consequence of the body's rotation. A fluid body in hydrostatic equilibrium deforms to an
189 oblate (Maclaurin) spheroid. This feature would arise on a strengthless body, though
190 strength could permit some deviation from the equilibrium surface. In contrast, the ridge is
191 a much narrower, topographic feature superposed on top of the bulge. It is completely
192 supported by internal strength and is absent in the hydrostatic case.

193 As viewed from the pole, Bennu's equatorial ridge shows a squarish outline (see
194 Figure 1a). This deviation from circularity is caused by four north-south longitudinal ridges
195 (Barnouin et al. 2019). These ridges extend from pole to pole, although two of these are
196 obscured in the southern hemisphere by surface material (Daly et al., 2020). These ridges
197 are broad and contribute to the overall shape of Bennu rather than appearing as spines on
198 top of the background shape. The squarish outline of Bennu's equator is confirmed in
199 Figure 4. The red zones at the equator and yellow zones in mid-latitudes indicating higher
200 elevations are the expression of the longitudinal ridges in the shape model. In contrast, the
201 equatorial outline of Ryugu is nearly circular and deviates little from the mean radius,
202 except in a few places where large craters lie on the equatorial ridge (e.g., lower right of
203 Figure 4). Instead, Ryugu shows dramatic variations in the topography at mid- to high
204 latitudes. The mid-latitudes are not uniformly low relative to the spheroid as they nearly
205 always are for Bennu, but the northern hemisphere has two large depressions of ~100 m,
206 separated by a massive rise.

207 The deviation from the idealized surface can alternatively be described in terms of
208 the tilt of the surface. The term "tilt" here represents the angle between the normal to a
209 facet on the surface and the radial direction at that point. The tilt is thus a purely geometric

210 measure, in contrast to “slope,” which characterizes the orientation of a surface facet with
211 respect to the surface acceleration direction. In Figure 5, we show the tilts of the closest-fit
212 Maclaurin spheroid consistent with Bennu’s and Ryugu’s observed densities and rotation
213 rates (left) and the tilts of the shape models (right). The Maclaurin spheroids are symmetric
214 about the rotation axis and only have tilts in the north-south direction. For consistency, we
215 show the north-south component of the tilt for the actual shape models as the most relevant

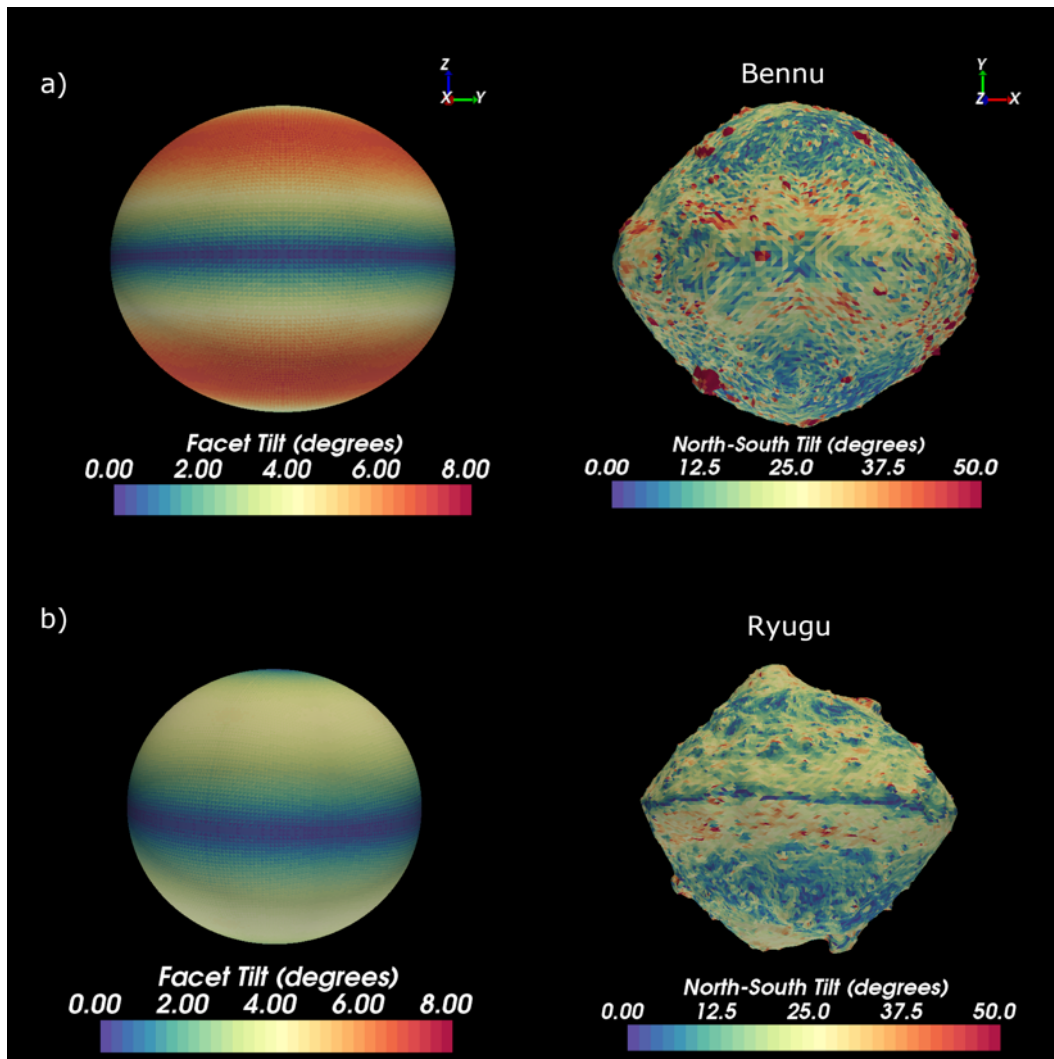


Figure 5: Component of tilts (angle between the normal to the surface and the direction to the center) in the north-south direction from closest-fit Maclaurin spheroids consistent with Bennu’s (a) and Ryugu’s (b) observed density and rotation period (left) and from the shape model (Bennu OLA v20; Ryugu v20190802) with 49,000 facets is shown. The maximum tilt shown is capped at 50° to highlight the average tilt distribution, but tilts exceed this in places on both asteroids.

216 deviation from the Maclaurin surface. These maps can be used to constrain the angle of
217 internal friction, which must be high enough to support material from sliding downslope
218 to meet the equilibrium surface. The maximum tilts on the shape model are at lower
219 latitudes than those on the Maclaurin surface and illustrate the flanks of the equatorial
220 ridge. In Figure 6, we show the number of facets on each body that exceed a certain tilt. It
221 is evident that although Bennu has more facets with extremely high tilts ($>30^\circ$) than Ryugu,
222 the median tilt is somewhat higher on Ryugu than on Bennu, largely in the vicinity of the
223 very large boulders at high latitudes. In places the tilt even exceeds 90° , where blocks have
224 overhanging ledges, which requires that these are fully intact, solid rocks. The equatorial
225 ridge on Ryugu is pronounced; a sharp contrast in tilt near the equator is clear, with a
226 narrow line of blue (low tilt) showing the peak of the ridge, surrounded by broad regions
227 of yellow (moderate tilt). In contrast, the tilts on Bennu rarely exceed the angle of repose,

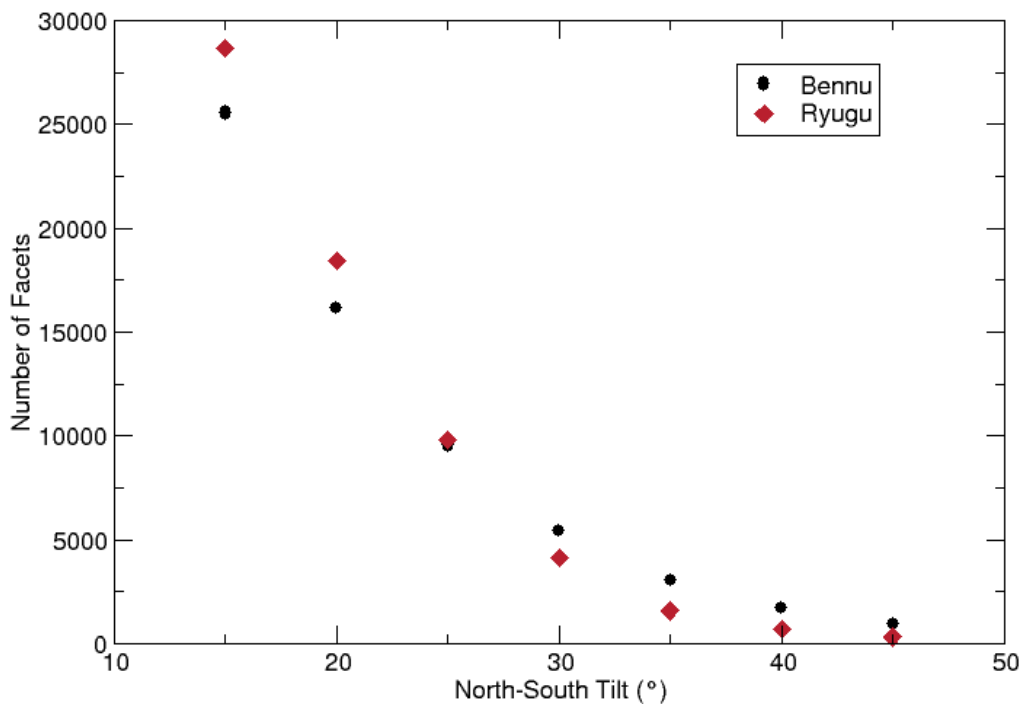


Figure 6: Number of facets on the 49,000-facet shape models of Bennu and Ryugu where the north-south tilt exceeds a given value.

228 and these regions are confined to the flanks of the equatorial ridge, which is far less defined
229 than on Ryugu. The tilts show a much more gradual transition from the flanks to the peak,
230 and the peak is broad. The larger tilts on Ryugu are even more pronounced when compared
231 to the tilts on the equivalent Maclaurin spheroid. Because Ryugu has a slower rotation rate,
232 it is less oblate, and the peak tilt on the spheroid is only half that of the equivalent spheroid
233 for Bennu.

234

235 **3. Spherical Harmonic Analysis**

236 We performed spherical harmonic decomposition of the shape models of Bennu
237 (SPC/OLA combined, v34) and Ryugu (SPC, v20190802) to interpret the geological
238 significance of their shapes. Because the two asteroids are roughly a factor of two different
239 in diameter, we used shape models with the same number of facets for each body (49,000)
240 rather than the same pixel scale. That is, the facets on each body are a similar fraction of
241 that body's surface area. The facets on Ryugu are therefore twice as large in an absolute
242 sense than those on Bennu. In Figure 7, we plot the orthonormalized RMS amplitude of all
243 zonal (black), sectoral (red), and tesseral (blue) terms at a given degree (ℓ). On both bodies,
244 the zonal terms (components that vary only with latitude) are particularly strong at $\ell = 2$
245 due to the equatorial bulge, and at $\ell = 4$, due to the equatorial ridge, that is characteristic
246 of top-shaped asteroids.

247 On Bennu, the zonal powers (components that vary only with latitude) at $\ell = 6$
248 and 8 are indicative of sharp regional changes in the slope, such as terraces (Barnouin et
249 al., 2019b; Daly et al., 2020). Strong sectoral terms at $\ell = 4$ reflect the aforementioned
250 high-standing longitudinal ridges (Barnouin et al., 2019a; Daly et al., 2020).

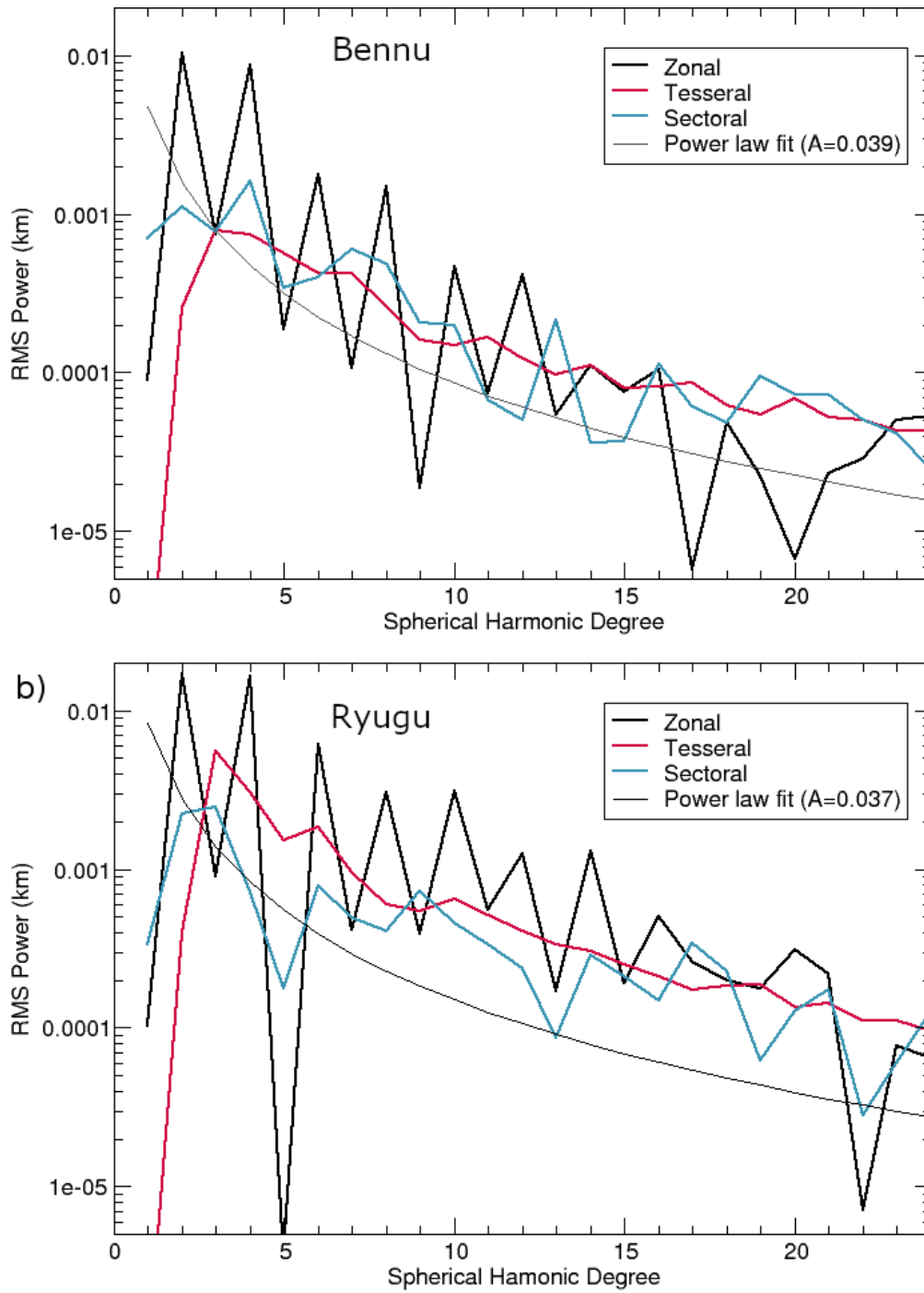


Figure 7: Spherical harmonic decompositions of the shapes of Bennu (a) and Ryugu (b), showing the total degree strength of the zonal, tesseral, and sectoral components on each body. A power-law fit (c.f., Vening-Meinesz, 1951) is also shown for comparison.

252 Apart from the top-like shape and the oscillation in the zonal harmonics, Ryugu
253 differs from Bennu in this analysis. The $\ell = 4$ sectoral component is much weaker on
254 Ryugu, and longitudinal ridges are not observed (Matsumoto et al., 2020). Viewed from
255 above the pole, the profile of Ryugu is more circular. The strongest non-zonal contributions
256 are the tesseral terms at $\ell = 3$, indicating some large-scale asymmetry, which is prominent
257 in topography relative to a reference shape model constructed from the even zonal
258 harmonics (Matsumoto et al., 2020). The “Western bulge” centered at 225°E, 10°S
259 (Hirabayashi et al., 2019), the Tokoyo/Horai Fossae system in the southern hemisphere and
260 a large plain in the northwestern mid-latitudes (Watanabe et al., 2019) are important
261 contributors to this shape. At smaller scales, terraces are not evident; regolith run-ups and
262 imbricated boulders are observed (Sugita et al., 2019).

263 On both bodies, zonal terms show a sharp dichotomy between the odd and even
264 terms. By itself, the strong power in the even zonal harmonics and the relatively weak
265 power in the odd terms does not necessarily indicate symmetry about the equator. In fact,
266 broad hemispheric differences can be seen in the shape of Bennu. The southern hemisphere
267 in particular appears rounder and more flattened near the pole, while the longitudinal ridges
268 appear more prominently in the northern hemisphere (Daly et al., 2020). As described for
269 Bennu in Daly et al. (2020), splitting the shape model at the equator can shed light on other
270 contributions. In this approach, two new shape models are then created by reflecting each
271 hemisphere about the equator, forming new asteroid shapes composed of either two
272 northern or two southern hemispheres, thus enforcing hemispheric symmetry in each
273 model. Using this technique, we created and performed spherical harmonic decomposition

274 of hemispherically symmetric shape models of Bennu and Ryugu, and we compared them
275 to each other and to the actual shapes of the asteroids.

276 In Figure 8, we show the sectoral harmonics (terms varying only with longitude)
277 for the actual shape of Bennu, the northern hemisphere, and the southern hemisphere.
278 Although the $\ell = 4$ sectoral term is strongest in the north, the power at this wavelength does
279 not vary much among the models. As reported by Daly et al. (2020), one reason that the
280 ridges are less apparent to the eye in the southern hemisphere is that surface material fills
281 in some of the sectors between the ridges to a greater degree than in the north. This subdues
282 the visual prominence of the longitudinal ridges; although they are present in the south,
283 they stand less high above the background surface. This contributes to the power at $\ell = 2$,
284 which in the southern hemisphere is roughly equivalent to $\ell = 4$ (Daly et al., 2020).

285 Another important variation is seen at $\ell = 5$, with nearly an order of magnitude
286 difference between the hemispheres. A closer inspection of the southern hemisphere
287 suggests a component of five-fold (rather than four-fold) symmetry. A geological
288 interpretation consistent with both the surface observations and the spherical harmonic
289 decompositions is that in the southern hemisphere, one of the longitudinal ridges meanders
290 east and west from the equator to the pole. Although there are four ridges, the spacing
291 between them varies, shifting some of the power from degree 4 to adjacent degrees.

292 Ryugu does not show consistent power between the hemispheres at $\ell = 4$ or at any
293 other wavelength. The northern hemisphere is dominated by an $\ell = 2$ pattern in the shape
294 (an elongation in one direction), whereas the southern hemisphere shows a spike at $\ell = 4$

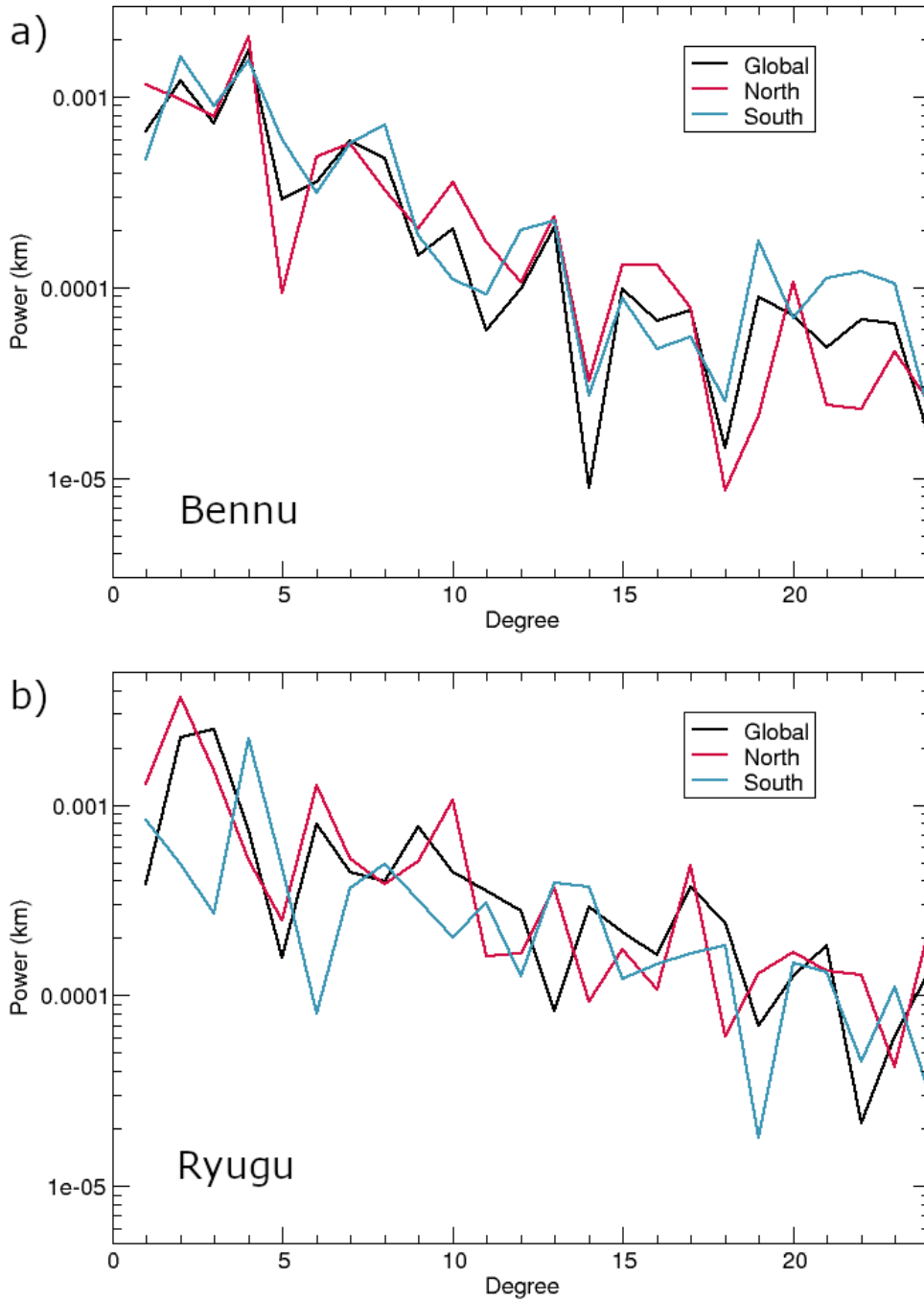


Figure 8: RMS amplitude in the sectoral harmonics in the OLA shape model (v14) for Bennu and the SPC shape model for Ryugu. For each body, the global results (black), northern (red) and southern (blue) hemispheres are shown.

295 that reflects the boulder distribution. At shorter wavelengths, the power in the spherical
 296 harmonics in each hemisphere is essentially independent of the other, and we interpret this

297 as a reflection of the distribution of large craters, which are more pronounced than on
298 Bennu.

299 These examples demonstrate the power of analyzing the shape in the spectral
300 domain. Patterns are revealed in the spherical harmonics that are less obvious by inspection
301 of the shape model that once known, can guide further geological analysis.

302

303 **4. Internal Properties**

304 The large-scale surface topography and rotation rates provide insight to the
305 interior structures of the asteroids. Although both objects appear to be unconsolidated
306 rubble piles, Bennu cannot be completely strengthless. As discussed above, Bennu's
307 rotation rate is significantly faster than any hydrostatic body could sustain (Figure 2).
308 Therefore, Bennu must have some internal stiffness (Barnouin et al., 2019a).

309 Beyond this broad observation, knowledge of the interior structure remains
310 somewhat speculative. However, we can use the constraints we do have to construct a
311 base model that is consistent with the existing observations. One such possibility is that
312 the longitudinal ridges may be the surface expression of an arrangement of about four
313 large (~100-m) fragments that make up the core of the asteroid, which is filled in and
314 covered by smaller rubble. Studies of rotational failure of rubble piles (Zhang et al.,
315 2018) have found that a common result is for the body to fail in a wedge-shaped pattern,
316 with the number of wedges controlled by the cohesion of the material. Although even
317 homogenous interiors can fail in a wedge-shaped pattern, having some coherent large
318 fragments in the interior could simulate a high cohesion.

319 We have illustrated this scenario in Figure 9. Here, the large clasts are prolate and
320 would naturally arrange themselves into a cluster, all oriented the same direction. These
321 large fragments are effectively zones of extremely high cohesion and would direct failure
322 to occur primarily in a $\ell = 4$ pattern. The fragments would anchor the wedges, and the
323 longitudinal ridges would correspond to their centers (Daly et al., 2020). Although Figure
324 9 is conceptual, we can compare characteristics to the interior structure inferred from the
325 gravity solution from OSIRIS-REx observations. The above scenario contains an under-
326 dense core and equator, where the smaller rubble and void spaces are most prevalent. In

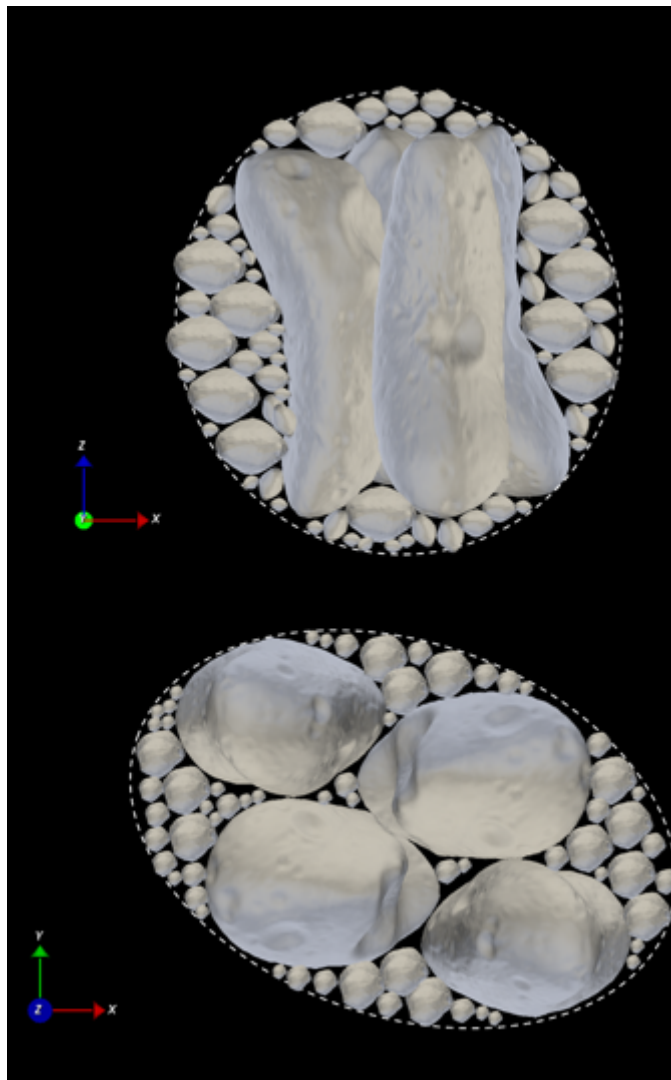


Figure 9: Possible internal structure of Bennu viewed from the equator (top) and the pole (bottom). Four large prolate clasts form the bulk of the interior, and are filled in by smaller rubble.

327 that regard, it is consistent with the gravity field of Bennu, which points to a
328 heterogeneous mass distribution (Scheeres et al., 2020).

329 If these larger clasts have some inherent tensile strength, they would resist
330 deformation themselves, and could lock up the smaller rubble, limiting deformation of
331 the asteroid overall. Surface landslides would still occur. It is possible that terraces on
332 Bennu (Barnouin et al., 2019b) are the expression of downslope migration of material as
333 the increasing rotation rate mobilized it. We note that the scenario presented here is a
334 hypothesis, and that alternative models to explain the shape could be proposed.

335 The fact that terraces are not observed on Ryugu (Matsumoto et al., 2020) could
336 simply be a consequence of Ryugu's slower rotation. However, if Ryugu previously had
337 a higher spin rate, that could have triggered the formation of terraces during that era,
338 which may have remained after spin-down. Thus, the absence of terraces may be an
339 indication that the mechanical response of the surface on Ryugu is different than on
340 Bennu. This, in addition to the lumpier shape of Ryugu, points to a different
341 configuration of large central clast; to the possibility that Ryugu has no larger pieces in
342 the center and is uniform rubble throughout; or to an entirely different mixture. For
343 example, Ryugu's western bulge (Hirabayashi et al., 2019) may indicate a large fragment
344 in the shallow subsurface rather than the center.

345

346 **5. Spin Evolution**

347 The configuration of rubble in the asteroid interior and the distribution of material
348 on the asteroid surface may have implications for the spin evolution of asteroids such as
349 Bennu and Ryugu. For example, the magnitude of YORP-induced torque is sensitive to

350 the orientation of blocks on the surface (Rubincam, 2000; Statler, 2009). Using the shape
 351 models of Bennu (OLA v16) and Ryugu (v20190802), and following Rubincam (2000),
 352 we compute the amount of solar energy on each facet of the shape model:

$$353 \quad SdA = (\hat{r}_S \cdot \hat{N})F_s dA$$

354 where S is the insolation, dA is the area of the facet, F_s is the solar power per unit area,
 355 and $\hat{r}_S \cdot \hat{N}$ is the component of the surface normal of that facet in the direction of the Sun.
 356 We assume the facet is in radiative steady state, and following Lambert's law, the net
 357 force per unit area \vec{f} on the facet is:

$$358 \quad \vec{f} = \frac{-2 S \hat{N} F_s}{3c}$$

359 where c is the speed of light. The torque on the facet is a product of the applied force and
 360 the distance from the center of mass, \vec{r} .

$$361 \quad d\vec{\tau} = \vec{r} \times \vec{f} dA$$

362 We sum over all the facets to determine the net torque on the body. We then rotate the
 363 body 5° about its axis, identify the new subsolar point, and recalculate. The calculation is
 364 repeated every 5° of rotation to determine the net and average torque over one full
 365 rotation. We repeat this iteration for every 5° of true anomaly to determine the net and
 366 average torque over one full orbital period.

367 In Figure 10, we show the total YORP torques about the rotational axis averaged
 368 over the body and over one rotation as a function of the true anomaly (orbital position)
 369 for Bennu and Ryugu. The rotational torque on Ryugu oscillates over the course of one
 370 orbital period, whereas the rotational torque on Bennu is consistently in one direction.
 371 Although the magnitude of the torque on Ryugu is ~ 3 times that on Bennu, Ryugu's

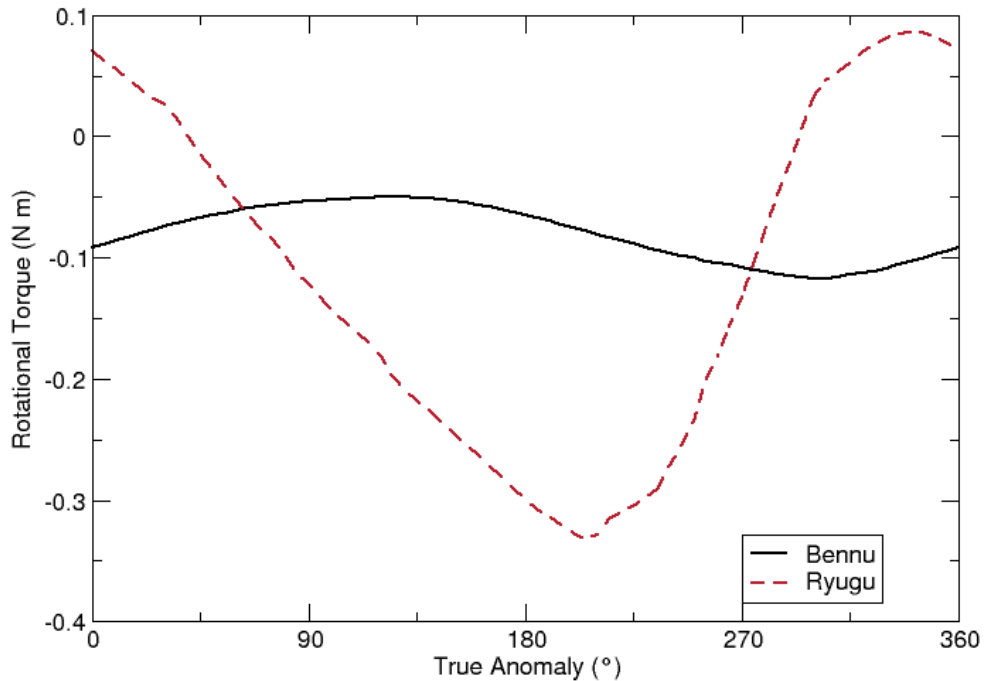


Figure 10: Rotational component of the YORP-induced torque on Bennu and Ryugu. In both cases, the highest-resolution shape models (with 3 million facets) were used.

372 moment of inertia is roughly 20 times that of Bennu, so the net rate of predicted change
 373 in angular velocity is substantially larger on Bennu than on Ryugu.

374 Although the YORP effect may be sensitive to small-scale topography (Statler,
 375 2009), if the distribution of blocks on the surface has a truly random orientation, then the
 376 torques from individual surface facets should cancel each other out. Over a long timescale
 377 (greater than an orbital period), the average torque due to small-scale features on a rubble
 378 pile should average to zero. For this reason, it has been suggested that long-wavelength
 379 topography is the driver of YORP torques (Rubincam, 2000). Thus, a sustained change in
 380 rotation rate due to the YORP effect would require a systematic preference in the
 381 orientation of the topography that is not likely to be caused by small-scale processes.
 382 However, recent work (e.g., Statler, 2009; Rozitis and Green, 2012; Golubov and Krugly,
 383 2012; Nolan et al., 2019) have shown that small-scale topography may be potentially
 384 significant, and we explore wavelength dependence in the following section.

385

386 *5.1 Long-wavelength topography and the spin up of Bennu.*

387 We can examine the effects of the longest wavelengths by decomposing a shape
388 model into its spherical harmonic components and then creating partial reconstructions of
389 that shape out to a chosen spherical harmonic degree and order. Ground-based, Hubble
390 Space Telescope, and OSIRIS-REx spacecraft observations of Bennu have shown that its
391 rotation rate has been increasing since 1999 (Hergenrother et al., 2013, Nolan et al., 2013;
392 Lauretta et al., 2015; Nolan et al., 2019; Hergenrother et al., 2019). Similar rotation rate
393 changes have not been observed for Ryugu, and would not be expected because of the
394 shorter observational baseline. Therefore, in the following analysis, we focus exclusively
395 on Bennu.

396 We used the 12-m-resolution v34 shape model of Bennu generated from the
397 combination of SPC and OLA data. In Figure 11, we show reconstructions of Bennu out
398 to degrees 4 and 8. The $\ell = 4$ reconstruction accentuates the top-like shape in the equatorial
399 views (panels a to d). The profile of the equator as seen in the polar views (panels e and f)
400 is noncircular. The actual profile is intermediate between these, where the “corners”
401 indicate the longitudinal ridges. The degree 8 reconstruction (the first harmonic of degree
402 4) in Figure 11g–l shows that an octagonal fit is better and that there is a weaker set of
403 longitudinal features at degree 8 contributing to the shape.

404 We hypothesize that the longitudinal ridges observed on Bennu may promote spin-
405 up preferentially in one direction about the rotation axis, like the blades on a windmill. Not
406 only do these ridges constitute systematic long-wavelength topography, but they also
407 control the distribution of smaller rubble. In contrast, Ryugu, which does not exhibit signs

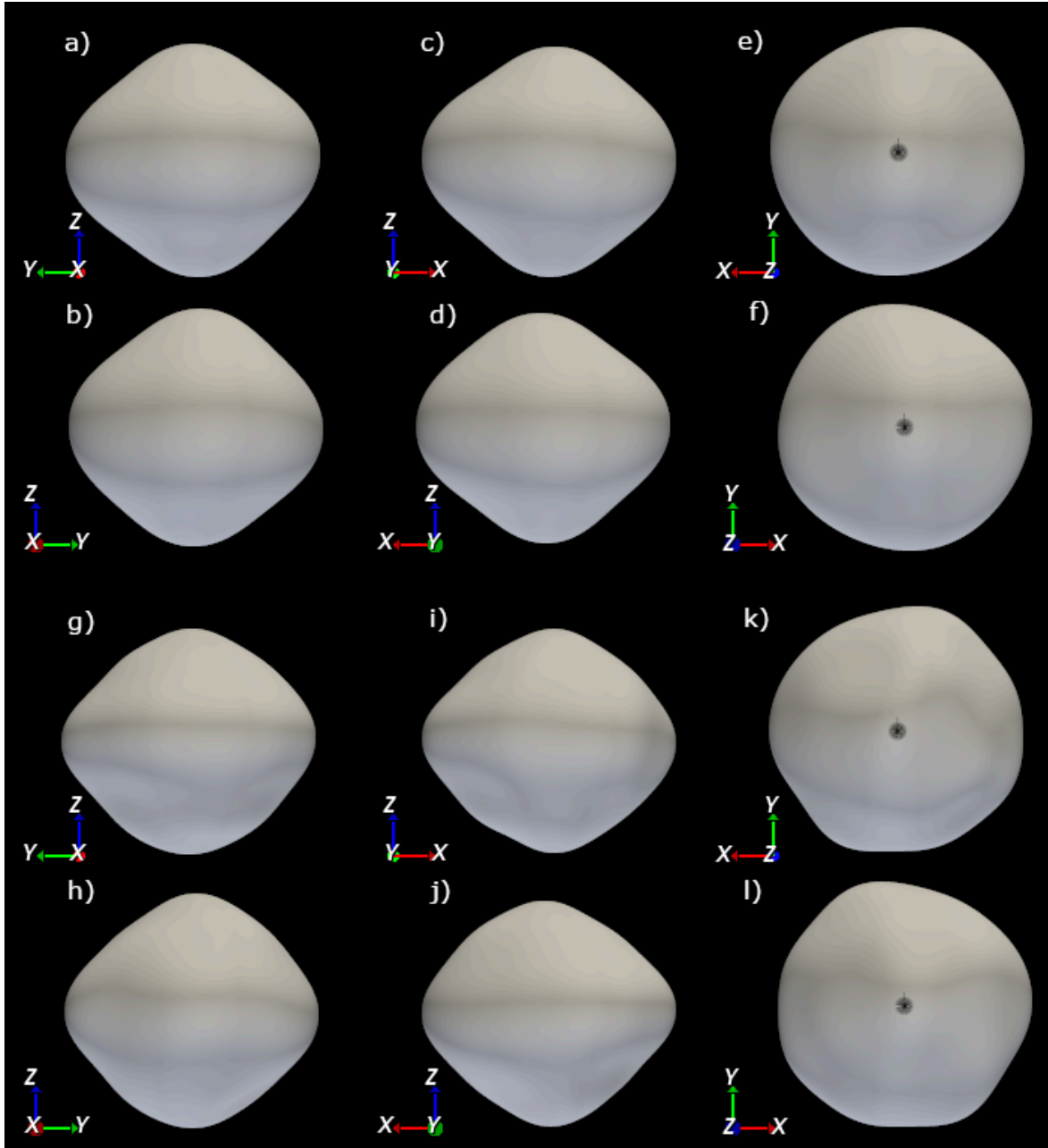


Figure 11: Reconstruction of Bennu shape model out to degree and order 4 as seen from the $+x$ (a), $-x$ (b), $+y$ (c), $-y$ (d), $+z$ (e), and $-z$ (f) axes; to degree and order 8 as seen from the $+x$ (g), $-x$ (h), $+y$ (i), $-y$ (j), $+z$ (k), and $-z$ (l) axes.

408 of significant YORP spin-up, lacks these ridges, and the rubble is distributed in a more
 409 random configuration, which is less susceptible to YORP spin-up.

410 To test this hypothesis, we decomposed the full shape model of Bennu (SPC/OLA
 411 v34) into spherical harmonics out to degree and order 48 and created a series of shape

412 reconstructions containing only selected spherical harmonic components. We then repeated
413 our torque calculation on the reconstructed shape models to determine which spherical
414 harmonic components were the dominant contributors to the spin evolution. The torque
415 computed on the appropriate partial reconstruction should approximate that on the full
416 shape model.

417 Torque is a vector and has a rotational component (aligned with the rotational axis),
418 which serves to change the body's rotation rate, and transverse components (perpendicular
419 to the rotational torque) that change the body's obliquity. Because Bennu's obliquity is
420 nearly 180° , the rotation axis is almost aligned with the direction of the solar radiation. The
421 zonal terms (which vary only with latitude), therefore, contribute most to the transverse
422 torque, and have a minimal effect on the rotational component. Because the spin is
423 controlled by the rotational torque, the most relevant spherical harmonics would be the
424 sectoral terms, which vary only with longitude. The most prominent feature in this
425 category are the longitudinal ridges, which are dominated by degree and order 4. Our first
426 partial reconstruction contains only the degree and order 4 term (superposed on a sphere of
427 the mean radius). We find that this shape reconstruction produces only a fraction of the
428 torque as from the full shape model (Figure 12; compare black and red curves). The daily
429 averaged rotational torque on each facet on this shape model is shown in Figure 13a. This
430 result has a straightforward explanation. A net torque about the rotation axis requires that
431 solar re-emission be preferentially oriented in one direction. If the body is symmetrical
432 about the rotation axis, the torque sums to zero. If the longitudinal regions were a pure
433 sectoral harmonic, then each side of the ridge would re-emit sunlight equally efficiently,
434 and the torque applied to a ridge in the morning would be canceled by that applied in the

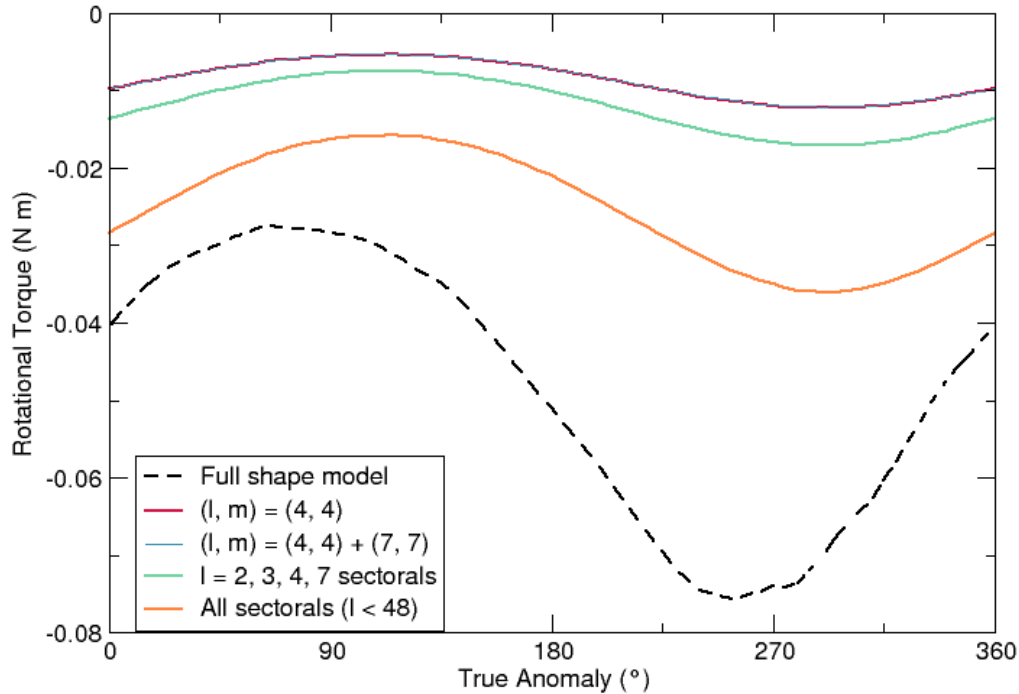


Figure 12: Globally averaged rotational component of YORP-induced torque as a function of orbital position on partial shape reconstructions of Bennu based on selected spherical harmonic terms. The (4,4) curve and (4,4) + (7,7) are nearly coincident.

435 afternoon. A shape model reconstruction with multiple components is therefore required
 436 to break the symmetry. In order to get this type of asymmetry, combinations of degrees
 437 much higher than the wavelength of the feature are required; this is analogous to the Gibbs'
 438 phenomena for Fourier series.

439 We next constructed a Bennu shape model with the sectoral terms at degrees 2, 3,
 440 4, and 7, the four largest such components. The total rotational torque on this shape model
 441 is only ~25% of the total on the full shape model (Figure 12, green curve), indicating that
 442 although these four components may be dominant, there is substantial contribution from
 443 other terms. The map of the torque computed on this model is shown in Figure 13b. Thus,
 444 although the long-wavelength features such as the longitudinal ridges may enable a
 445 systematic YORP spin-up, by themselves they cannot explain the magnitude of the net
 446 torque.

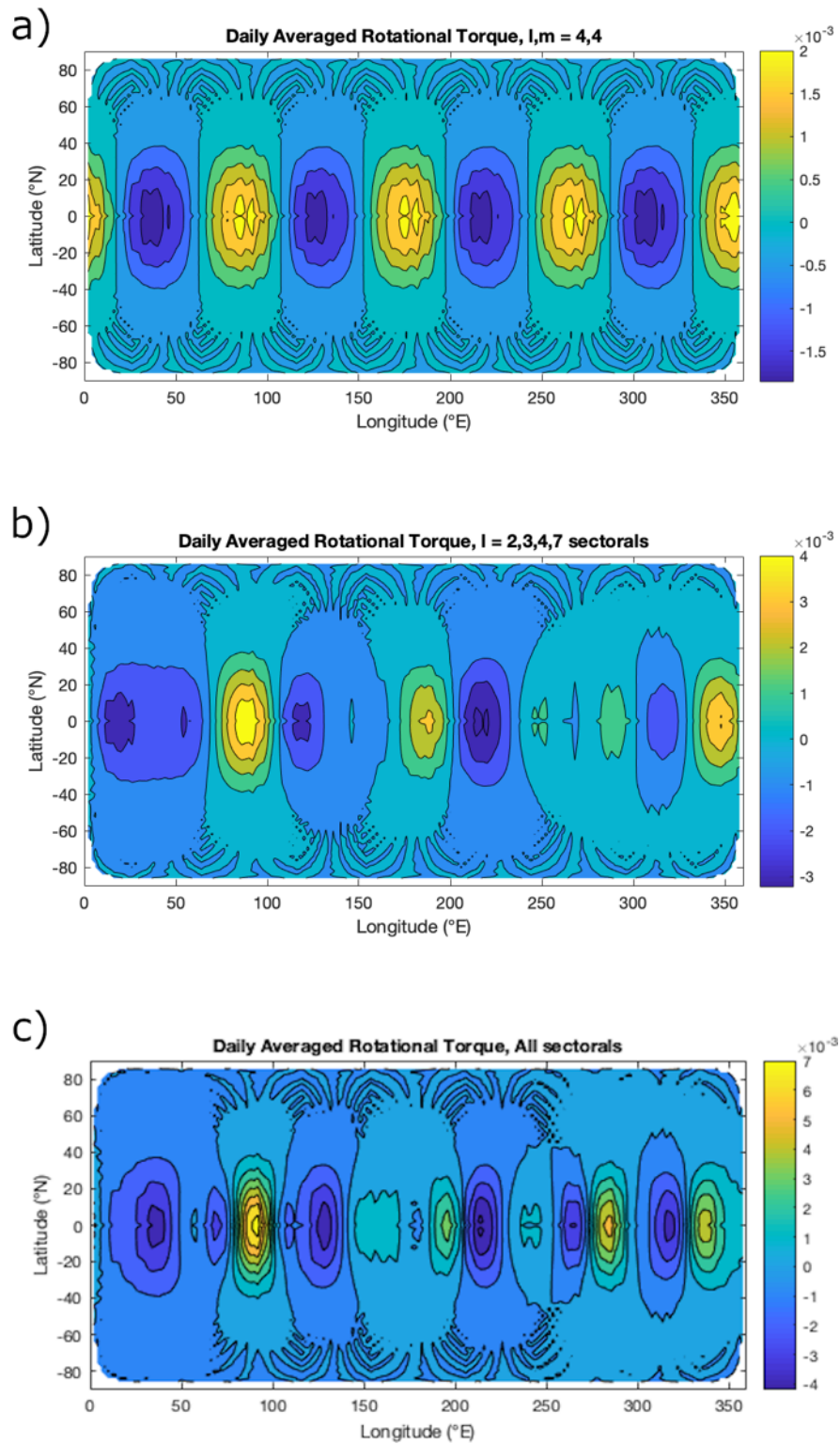


Figure 13: Daily averaged rotational torque (at a true anomaly of 180°) on a partial shape reconstruction of Bennu consisting of only the degree 0 and degree 4, order 4 components of topography (a); the degree 0 and degree 2, 3, 4, and 7 sectoral components of topography (b); and the degree 0 and all sectoral components of topography out to degree 48 (c) plotted in map projection (i.e., mean torque on each facet of the shape model, integrated over one full rotation).

448 We created another partial reconstruction that included all the sectoral components
 449 (out to degree 48; Figure 13c); it only results in ~50% of the total torque (Figure 12, orange
 450 curve), meaning that there is significant contribution from the tesseral terms as well. Table
 451 3 gives the globally averaged rate of change in rotation rate and obliquity, averaged over a
 452 Bennuvian year for each shape reconstruction, demonstrating that as additional terms are
 453 included, the total YORP effect increases. This result suggests that smaller-scale
 454 topography (< 15 m, $\ell > 100$) is important to the full solution and an important driver of
 455 YORP on Bennu. The YORP torques are only due to an effective area that is a fraction of
 456 the surface area because it is caused only by asymmetries. The effective area for YORP
 457 can increase as finer scales are considered if the topography is non-random and the
 458 asymmetries do not cancel each other.

459 The torque analysis shown here is valid only for the current shape of Bennu.
 460 Assuming that this shape remains constant, then the position of Bennu on the stability
 461 curves in Fig. 2 will continue to migrate upwards on the plot. If the observed rate of
 462 increase in the spin rate also remains constant, then in ~600 Myr, the spin rate will have

Table 3: YORP-induced change in rotation rate and obliquity for Bennu

Components	Rotational acceleration		Obliquity torque (N m)
	(s ⁻²)	(° day ⁻²)	
(4,4)	-3.61×10^{-18}	-1.54×10^{-6}	1.92×10^{-18}
(4,4); (7,7)	-3.65×10^{-18}	-1.56×10^{-6}	2.74×10^{-19}
(2,2); (3,3); (4,4); (7,7)	-4.99×10^{-18}	-2.13×10^{-6}	-3.36×10^{-18}
All sectorals ($\ell < 48$)	-1.04×10^{-17}	-4.45×10^{-6}	-5.92×10^{-18}
Full shape	-2.60×10^{-17}	-11.12×10^{-6}	-2.31×10^{-13}

463 increased to a level where no amount of internal friction would be sufficient to maintain a
464 rubble pile against disruption. Such a catastrophic scenario is unlikely. As the spin
465 increases slightly, the shape of the asteroid will be modified, and the rotational potential
466 will also increase. In the absence of internal strength, this potential serves to increase the
467 oblateness of the body, increasing the moment of inertia. As the oblateness increases, the
468 spin rate will go down by conservation of angular momentum of the system, preventing
469 unchecked spin-up (e.g., Walsh et al., 2008, 2012; Hirabayashi and Scheeres, 2015;
470 Scheeres et al., 2015).

471 In addition to tilts of the existing surface facets driven by this change in shape, any
472 rubble sitting on the surface with minimal cohesion will be disturbed and jostled into new
473 orientations. If these orientations are random, then these blocks may at times become more
474 susceptible to YORP, and at other times, less susceptible. Over long timescales, the body
475 would experience a YORP “random walk” rather than a YORP spin-up (Cotto-Figueroa et
476 al., 2015), wherein minor mass movements result in random shifts in the orientation of the
477 surface. The net effect of YORP would be to increase or decrease the rotation rate of the
478 asteroid in a stochastic fashion. If, however, there are large-scale structures (e.g., the
479 longitudinal ridges) that control the distribution and orientation of the rubble, then it may
480 be susceptible to prolonged spin-up or spin-down, and this would be deterministic.

481 A further caveat to the analysis presented here is that we have considered only the
482 normal torque due to YORP. Golubov and Krugly (2012) have suggested that asymmetric
483 re-radiation from smaller (few centimeters-sized) rocks could create a substantial
484 component of torque normal to the surface, called “tangential” YORP, modifying the
485 YORP in certain circumstances. Although the images of Ryugu and Bennu can resolve

486 features of a few centimeters in size, creating a global shape model on this scale is not
487 currently feasible. Surface roughness (on a scale as fine as millimeters) can also dampen
488 the degree of rotational acceleration. Radiation off such small-scale features is similar to
489 scattered light. Identification of the dominant scattering direction is needed to estimate
490 the influence of YORP at the finest scales. Rozitis (2016) found that the degree of
491 rotational acceleration due to the YORP effect can be dampened by a factor of $\sim 1/3$
492 through the thermal beaming effect, in which multiple scatterings of radiation between
493 surface elements can absorb more solar radiation than a flat surface, and reflect much of
494 it back towards the Sun.

495

496 **6. Conclusions**

497 We performed a topographic analysis of the shapes of the top-shaped rubble-pile
498 asteroids Ryugu and Bennu, which were each recently visited. Although the two bodies
499 appear similar, spherical harmonic analysis of the shapes demonstrates differences, in
500 particular a much sharper equatorial ridge on Ryugu than on Bennu, and longitudinal ridges
501 and terraces on Bennu that are absent on Ryugu.

502 We find that both objects are rotating at a rate exceeding that at which a Maclaurin
503 spheroid would be stable, indicating that some degree of internal friction or cohesion is
504 necessary to maintain their current shapes. Bennu rotates considerably faster than Ryugu
505 and requires a friction angle of at least 17° in the absence of cohesion to maintain itself
506 against despinning or disruption. In contrast, Ryugu requires only $\sim 3^\circ$ of internal friction
507 to be stable against the rotation. This result is reflected in the differences in the tilt maps
508 of each asteroid. Ryugu on average has higher tilts than Bennu and a more prominent

509 equatorial ridge, suggesting that the original top shape has been less modified by, for
510 example, rotational migration than has Bennu's. The interior strength inferred here for
511 Bennu ($>17^\circ$ internal friction) is similar to that of Itokawa, another rubble-pile asteroid
512 (Fujiwara et al., 2006) of similar size to Bennu. The other prolate asteroids studied here do
513 not require similar levels of strength (though nothing precludes their having it).

514 The longitudinal ridges on Bennu may indicate some large-scale strength and
515 structure in the interior and hint at a failed disruption event earlier in the body's history
516 (Daly et al., 2020). The longitudinal ridges may themselves enable YORP spin-up (or spin-
517 down), although on their own they are not sufficient to achieve this. The torque computed
518 on partial shape reconstructions shows that smaller-scale topography (<15 m) is important.
519 Sustained YORP spin-up would require that the smaller rubble be either systematically
520 oriented in a particular direction or non-uniformly rather than randomly distributed, and
521 this requires models of the deformation of the asteroid as a result of the rotational potential.
522 Because a given topographic feature creates more torque the further it is from the origin,
523 small-scale features on the ridges are more important than those between the ridges. Thus,
524 the ridges are critical in directing the YORP torque, even if they themselves only contribute
525 a fraction of the total. A sustained period of spin-up would require the body to have
526 sufficient internal strength that it would not substantially deform and redistribute surface
527 rubble in response to small increases in rotation rate. The fact that Ryugu does not exhibit
528 a similar rotational evolution to Bennu may point to either a lack of topographic features
529 to promote the YORP effect, a lack of strength to sustain it, or both. However, Ryugu has
530 a much slower rotation period and larger size than Bennu, which decreases the importance
531 of shape to the rotational history. A change in Ryugu's rotation rate due to YORP may

532 simply not be detectable in the available data. Given these factors, we refrain from drawing
533 conclusions on the effect of shape on the YORP effect for Ryugu.

534

535 **Acknowledgments**

536 This material is based upon work supported by NASA under Contract NNM10AA11C
537 issued through the New Frontiers Program. The OSIRIS-REx Laser Altimeter build and
538 Canadian science support were provided by a contract with the Canadian Space Agency.
539 P.M. and Y.Z. acknowledge funding support from the French space agency CNES,
540 from the European Union's Horizon 2020 research and innovation programme under grant
541 agreement no. 870377 (project NEO-MAPP) and from the Academies of Excellence on
542 Complex Systems and Space, Environment, Risk and Resilience of the Initiative
543 d'EXcellence "Joint, Excellent, and Dynamic Initiative" (IDEX JEDI) of the Université
544 Côte d'Azur. Y. Z. acknowledges funding from the Université Côte d'Azur "Individual
545 grants for young researchers" program of IDEX JEDI.

546 We thank two anonymous reviewers for insightful reviews which helped to improve
547 the manuscript clarity and quality. We are grateful to the entire OSIRIS-REx and
548 Hayabusa2 Teams for making the encounters with Bennu and Ryugu possible. This work
549 made use of the Small Body Mapping Tool (SBMT), a free spacecraft data visualization
550 and analysis tool developed at the Johns Hopkins University Applied Physics Laboratory
551 (Ernst et al., 2018); visit sbmt.jhuapl.edu to learn more and for access to shape models of
552 Bennu.

553

554 **References**

- 555 Barnouin, O.S. et al. (2019a), Shape of (101955) Bennu indicative of a rubble pile with
556 internal stiffness, *Nat. Geosci.*, *12*, 247–252.
- 557 Barnouin, O.S. et al. (2019b), On the possible origin of terraces on Bennu, *EPSC-DPS*
558 Abstract #2019-255.
- 559 Barnouin, O.S. et al. (2020). Digital terrain mapping by the OSIRIS-REx mission, *Planet.*
560 *Space Sci.* *180*, 104764.
- 561 Cotto-Figueroa, D., Statler, R. S., Richardson, D. C., Tanga, P. (2015), Coupled spin and
562 shape evolution of small rubble-pile asteroids: Self-limitation of the YORP effect,
563 *Astropys. J.* *803*:25.
- 564 Daly, M.G., Barnouin, O. S., Dickinson, C., Seabrook, J., Johnson, C.L., Cunningham,
565 G., Haltgin, T., Gaudreau, D., Brunet, C., Aslam, I., Taylor, A., Bierhaus, E. B.,
566 Boynton, W., Nolan, M., Lauretta, D. S. (2017), The OSIRIS-REx Laser Altimeter
567 (OLA) Investigation and Instrument, *Space Sci. Rev.*, *212*, 899–924.
- 568 Daly, M.G. et al., (2020), Hemispherical Differences in the Shape and Topography of
569 Asteroid (101955) Bennu, *Science Advances*, 10.1126/sciadv.abd3649
- 570 Das, B.M. (2010), *Principles of geotechnical engineering*, 7th edn. Cengage Learning,
571 Stamford, CT.
- 572 Delbo, M. et al. (2014), Thermal fatigue as the origin of regolith on small asteroids.
573 *Nature*, *508*(7), 233–236.
- 574 DellaGiustina, D. N., Emery, J. P., et al. (2019), Properties of rubble-pile asteroid
575 (101955) Bennu from OSIRIS-REx imaging and thermal analysis, *Nat. Astron.*, *3*,
576 341–351.

577 Dombard, A.J., Barnouin, O.S., Prockter, L.M., Thomas, P.C. (2010), Boulders and
578 ponds on the Asteroid 433 Eros, *Icarus*, 210, 713–721.

579 Ernst et al., 2018, The Small Body Mapping Tool (SBMT) for Accessing, Visualizing,
580 and Analyzing Spacecraft Data in Three Dimensions, LPSC 49, abstract no. 1043.

581 Farnham, T.L., SHAPE MODEL OF ASTEROID 21 LUTETIA, RO-A-
582 OSINAC/OSIWAC-5-LUTETIA-SHAPE-V1.0, NASA Planetary Data System,
583 2013.

584 Gaskell, R.W., Gaskell Eros Shape Model V1.0. NEAR-A-MSI-5-EROSHAPE-V1.0.
585 NASA Planetary Data System, 2008.

586 Gaskell, R., Saito, J., Ishiguro, M., Kubota, T., Hashimoto, T., Hirata, N., Abe, S.,
587 Barnouin-Jha, O., and Scheeres, D., Gaskell Itokawa Shape Model V1.0. HAY-A-
588 AMICA-5-ITOKAWASHAPE-V1.0. NASA Planetary Data System, 2008a.

589 Gaskell, R.W., Barnouin-Jha, O.S., Scheeres, D.J., Konopliv, A.S., Mukai, T., Abe, S.,
590 Saito, J., Ishiguro, M., Kubota, T., Hashimoto, R., Kawaguchi, J., Yoshikawa, M.,
591 Shirakawa, K., Kominato, T., Hirata, N., Demura, H. (2008b), Characterizing and
592 navigating small bodies with imaging data, *Meteorit. Planet. Sci.*, 43, 1049–1061.

593 Gaskell, R.W., 2013-02-13 Final Claudia Model., GASKELL_CLAUDIA_2013_02_13
594 NASA Planetary Data System, 2013.
595 http://dawndata.igpp.ucla.edu/tw.jsp?section=geometry/ShapeModels/GASKELL_C
596 [LAUDIA_2013_02_13](http://dawndata.igpp.ucla.edu/tw.jsp?section=geometry/ShapeModels/GASKELL_C)

597 Golubov, O., Krugly, Y. N. (2012), Tangential component of the YORP effect,
598 *Astrophys. J.* 752, L11.

599 Hamilton, V.E. et al. (2019). Evidence for widespread hydrated minerals on asteroid
600 (101955) Bennu. *Nat. Astron.* 3, 332–340.

601 Harris, A.W., Fahenstock, E.G., Pravec, P. (2009), On the shapes of “rubble pile”
602 asteroids, *Icarus* 199, 310–318.

603 Hergenrother, C. W., Nolan, M. C., Binzel, R. P., Cloutis, E. A., Barucci, M. A., Michel,
604 P., Scheeres, D. J., d'Aubigny, C. D., Lazzaro, D., Pinilla-Alonso, N., Campins, H.,
605 Licandro, J., Clark, B. E., Rizk, B., Beshore, E. C., & Lauretta, D. S. (2013).
606 Lightcurve, color and phase function photometry of the OSIRIS-REx target asteroid
607 (101955) Bennu. *Icarus*, 226, 663–670.

608 Hergenrother, C.W. et al. (2019), The operational environment and rotational
609 acceleration of asteroid (101955) Bennu from OSIRIS-REx observations. *Nature*
610 *Communications*, 10(1), 1291.

611 Hirabayashi, M., Scheeres, D.J. (2015), Stress and failure analysis of rapidly rotating
612 asteroid (29075) 1950 DA, *Astrophys. J. Lett.*, 798, L8.

613 Hirabayashi, M., Scheeres, D.J. (2019), Rotationally induced failure of irregularly shaped
614 asteroids, *Icarus* 317, 354-364.

615 Hirabayashi, M. et al. (2019), The Western Bulge of 162173 Ryugu Formed as a Result
616 of a Rotationally Driven Deformation Process, *Astrophys. J. Lett.* 874, L10.

617 Holsapple, K.A. (2004), Equilibrium figures of spinning bodies with self-gravity, *Icarus*,
618 172, 272-303.

619 Hirata, N. et al. (2018), Initial results of shape modeling on the asteroid Ryugu from
620 observations by Hayabusa2 for landing site selection, *DPS* 50, Abstract #501.05.

621 Jawin, E.R. et al. (2020). Global Patterns of Recent Mass Movement on Asteroid
622 (101955) Bennu. *J. Geophys. Res.* 125, e2020JE006475.

623 Kanamaru, M., Sasaki S., Wieczorek, M. (2019), Density distribution of asteroid 25143
624 Itokawa based on smooth terrain shape, *Planet. Space Sci.* 174, 32–42.

625 Lauretta, D. S., Bartels, A. E., Barucci, M. A., Bierhaus, E. B., Binzel, R. P., Bottke, W.
626 F. Jr., Campins, H., Chesley, S. R., Clark, B. C., Clark, B. E., Cloutis, E. A.,
627 Connolly, H. C., Crombie, M. K., Delbó, M., Dworkin, J. P., Emery, J. P., Glavin, D.
628 P., Hamilton, V. E., Hergenrother, C. W., Johnson, C. L., Keller, L. P., Michel, P.,
629 Nolan, M. C., Sandford, S. A., Scheeres, D. J., Simon, A. A., Sutter, B. M.,
630 Vokrouhlický, D., & Walsh, K. J. (2015). The OSIRIS-REx target asteroid (101955)
631 Bennu: Constraints on its physical, geological, and dynamical nature from
632 astronomical observations. *Meteorit. Planet. Sci.*, 50, 834–849.

633 Lauretta, D.S., DellaGiustina, D.N. et al. (2019). The unexpected surface of asteroid
634 (101955) Bennu. *Nature* 568, 55–60.

635 Matsumoto, K. et al. (2020), Improving Hayabusa2 trajectory by combining LIDAR data
636 and a shape model *Icarus*, 338, 113574.

637 Michel, P., Ballouz, R.-L., Barnouin, O.S., Jutzi, M., Walsh, K.J., May, B.H., Manzoni,
638 C., Richardson, D.C., Schwartz, S.R., Sugita, S., Watanabe, S., Miyamoto, H.,
639 Hirabayashi, M., Bottke, W.F., Connolly Jr., H.C., Yoshikawa, M., Lauretta, D.S.
640 (2020), Collisional formation of top-shaped asteroids and implications for the origins
641 of Ryugu and Bennu. *Nature Communications*, 11, 2665.

642 Molaro, J.L. et al. (2020), In situ evidence of thermally induced rock breakdown
643 widespread on Bennu’s surface. *Nature Communications* 11, 2913.

644 Nolan, M. et al. Shape model and surface properties of the OSIRIS-REx target asteroid
645 (101955) Bennu from radar and lightcurve observations (2013). *Icarus* 226, 629–
646 640.

647 Nolan, M.C., Howell, E.S., Scheeres, D.J., McMahon, J.W., Golubov, O., Hergenrother,
648 C.W., Emery, J.P., Noll, K.S. Chesley, S.R., Lauretta, D.S. (2019), Detection of
649 Rotational Acceleration of Bennu Using HST Light Curve Observations, *Geophys.*
650 *Res. Lett.*, 49, 1956–1962.

651 Ostro, S.J., Margot, J.-L., Benner, L.A.M., Giorgini, J.D., Scheeres, D.J., Fahnestock,
652 E.G., Broschart, S.B., Bellerose, J., Nolan, M.C., Magri, C., Pravec, P., Scheirich, P.,
653 Rose, R., Jurgens, R.F., De Jong, E.M., Suzuki, Shigeru (2006), Radar Imaging of
654 Binary Near-Earth Asteroid (66391) 1999 KW4, *Science*, 314, 1276–1280.

655 Richardson, J.E. and Bowling, T.J. (2014), Investigating the combined effects of shape,
656 density, and rotation on small body surface slopes and erosion rates. *Icarus*, 234, 53–
657 65.

658 Rozitis B., 2016, The surface roughness of (433) Eros as measured by thermal-infrared
659 beaming, *Mon. Not. R. Soc. Astron.*, 464, 915–923.

660 Rozitis B., Green S. F., 2012, The influence of rough surface thermal-infrared beaming
661 on the Yarkovsky and YORP effects, *Mon. Not. R. Astron. Soc.*, 423, 367–388.

662 Rubincam, D.P. (2000), Radiative Spin-up and Spin-down of Small Asteroids, *Icarus*,
663 148, 2–11.

664 Scheeres, Daniel J. Landslides and mass shedding on spinning spheroidal
665 asteroids. *Icarus* 247 (2015): 1-17.

666 Scheeres, D. J. et al. (2019), The dynamic geophysical environment of (101955) Bennu
667 based on OSIRIS-REx measurements. *Nat. Astron.* 3, 352–361.

668 Scheeres, D. J. et al. (2020), Heterogenous mass distribution of the rubble-pile asteroid
669 (101955) Bennu, *Science Advances*, 10.1126/sciadv.abc3350.

670 Statler, T. S. (2009), Extreme sensitivity of the YORP effect to small-scale topography,
671 *Icarus*, 202, 502–513.

672 Stooke, P., Stooke Small Body Shape Models V1.0. EAR-A-5-DDR-STOOKE-SHAPE-
673 MODELS-V1.0. NASA Planetary Data System, 2002.

674 Sugita, S. et al. (2019), The geomorphology, color, and thermal properties of Ryugu:
675 implications for parent-body processes, *Science*, 364, eaaw0422.

676 Vening-Meinesz, F.A. (1951), A remarkable feature of the Earth’s topography, *Prock. K.*
677 *Ned. Akad. Wet. Ser. B Phys. Sci.* 54, 212–228.

678 Walsh, K. J., Richardson, D. C. & Michel, P. (2008), Rotational breakup as the origin of
679 small binary asteroids. *Nature*, 454, 188–191.

680 Walsh, K.J. (2018), Rubble Pile Asteroids, *Ann. Rev. Astron. Astrophys.* 56, 593–624.

681 Walsh, K.J. et al. (2019), Craters, boulders and regolith of (101955) Bennu indicative of
682 an old and dynamic surface, *Nat. Geosci.*, 12, 242–246.

683 Walsh, K.J. et al. (2012), Physical Characterization and Origin of Binary Near-Earth
684 Asteroid (175706) 1996 FG₃, *Astrophys. J.*, 748, 104.

685 Watanabe, S., et al. (2019), Hayabusa2 arrives at the carbonaceous asteroid 162173
686 Ryugu - a spinning top-shaped rubble pile. *Science* 364, 268–272.

687 Zhang, Y., Richardson, D.C., Barnouin, O.S., Maurel, C., Michel, P., Schwartz, S.R.,
688 Ballouz, R.-L., Benner, L.A.M., Naidu, S.P., Li, J. (2017), Creep stability of the

689 proposed AIDA mission target 65803 Didymos: I. Discrete cohesionless granular
690 physics model, *Icarus*, 294, 98–123.
691 Zhang, Y. et al. (2018), Rotational failure of rubble-pile bodies: influences of shear
692 and cohesive strengths., *Ap. J.* 857, 15.